

Multicrystalline Informatics Applied to Multicrystalline Silicon for Unraveling the Microscopic Root Cause of Dislocation Generation

Kenta Yamakoshi, Yutaka Ohno,* Kentaro Kutsukake, Takuto Kojima, Tatsuya Yokoi, Hideto Yoshida, Hiroyuki Tanaka, Xin Liu, Hiroaki Kudo, and Noritaka Usami*

A comprehensive analysis of optical and photoluminescence images obtained from practical multicrystalline silicon wafers is conducted, utilizing various machine learning models for dislocation cluster region extraction, grain segmentation, and crystal orientation prediction. As a result, a realistic 3D model that includes the generation point of dislocation clusters is built. Finite element stress analysis on the 3D model coupled with crystal growth simulation reveals inhomogeneous and complex stress distribution and that dislocation clusters are frequently formed along the slip plane with the highest shear stress among twelve equivalents, concentrated along bending grain boundaries (GBs). Multiscale analysis of the extracted GBs near the generation point of dislocation clusters combined with ab initio calculations has shown that the dislocation generation due to the concentration of shear stress is caused by the nanofacet formation associated with GB bending. This mechanism cannot be captured by the Haasen-Alexander-Sumino model. Thus, this research method reveals the existence of a dislocation generation mechanism unique to the multicrystalline structure. Multicrystalline informatics linking experimental, theoretical, computational, and data science on multicrystalline materials at multiple scales is expected to contribute to the advancement of materials science by unraveling complex phenomena in various multicrystalline materials.

1. Introduction

Many of the metals, ceramics, semiconductors, polymers, and other materials used in our society are multicrystalline, and they are used in social infrastructure, making our lives more convenient and comfortable. Therefore, the question of how to improve the macroscopic performance of multicrystalline materials is ubiquitous in materials science. Multicrystalline material can be regarded as a very complex system consisting of many crystal grains of various orientations, sizes, and crystal defects such as grain boundaries (GBs) and dislocations. Their macroscopic properties depend significantly on the microstructures.^[1,2] The microstructures are highly dependent on the process conditions of how the material was made.^[3–5] Although much research and development have been done to realize multicrystalline materials with excellent performance and functionality, the fundamental question of designing the microstructure and what processes should be used to fabricate them is not fully answered.

K. Yamakoshi, T. Yokoi, H. Tanaka, X. Liu, N. Usami
 Graduate School of Engineering
 Nagoya University
 Nagoya 464–8603, Japan
 E-mail: usa@material.nagoya-u.ac.jp

Y. Ohno
 Institute for Materials Research
 Tohoku University
 Sendai 980–8577, Japan
 E-mail: yutaka.ohno.e6@tohoku.ac.jp

K. Kutsukake
 Center for Advanced Intelligence Project
 RIKEN
 Tokyo 103-0027, Japan
 T. Kojima, H. Kudo
 Graduate School of Informatics
 Nagoya University
 Nagoya 464–8601, Japan
 H. Yoshida
 SANKEN
 Osaka University
 Osaka 567-0047, Japan

 The ORCID identification number(s) for the author(s) of this article can be found under <https://doi.org/10.1002/adma.202308599>

© 2023 The Authors. Advanced Materials published by Wiley-VCH GmbH. This is an open access article under the terms of the Creative Commons Attribution-NonCommercial License, which permits use, distribution and reproduction in any medium, provided the original work is properly cited and is not used for commercial purposes.

DOI: [10.1002/adma.202308599](https://doi.org/10.1002/adma.202308599)

One of the reasons for this is that the complexity of the multicrystalline structure and the diversity of GBs make systematization difficult. Krause et al. pointed out that materials engineers need to collaborate with computer scientists, physicists, chemists, and cognitive scientists to advance understanding of GB property by developing a high throughput characterization technique, data acquisition tools, and methods to incorporate machine learning while considering the humans' strengths.^[6]

In fact, materials informatics, which accelerates materials development by linking experimental, theoretical, computational, and data science, has rapidly progressed and expanded from its focus on materials discovery orientation^[7–12] to multicrystalline materials, where complex and diverse structures have essential effects on their macroscopic properties. For example, in metallic materials, mechanical properties and the relationship between plastic deformation and stress concentration at grain boundaries are investigated by combining simulation on virtual 3D microstructures generated by Voronoi tessellation,^[13,14] molecular dynamics simulations^[15,16] or microstructural data measured by electron back-scattered diffraction^[17] with machine learning. Microstructure analysis methods that autonomously perform domain segmentation and clustering on 3D data have been proposed,^[18] making it possible to handle 3D structures of various materials as digital data.

Although it is not easy to collect a large amount of data from practical materials for 3D analysis, the application of photoluminescence (PL) imaging to multicrystalline silicon (mc-Si) wafers for practical solar cells, which captures the spatial distribution of electrical properties within a large-area substrate in a short time, has revolutionized research.^[19] Machine learning models have been created to predict solar cell performance from PL images of mc-Si wafers,^[20,21] which permitted instant materials selection and feedback to optimize the crystallization process. PL images of many mc-Si wafers sliced from the same brick have been reconstructed in 3D structures, which enabled statistical analysis of the growth behavior^[22] and visualization of generation, propagation, and annihilation of dislocation clusters.^[23–25]

We started a 6-year national project on “multicrystalline informatics” to reach solutions to the ubiquitous questions of how to improve the macroscopic performance of multicrystalline materials in 2017 using mc-Si as a model material. Silicon is a material composed of a single element with a relatively simple crystal structure, which limits the complex targets requiring data science, such as processing, analysis, and prediction of vast amounts of data, to the microstructure and GBs derived from multicrystalline materials. Furthermore, its attractive electrical, optical, and thermal properties have various device applications and promise to expand the methodology to understanding multiphysics involving carriers, light, and heat. We believe that if we can build a solid research base and academic theory using mc-Si as a model material, we can extend it to other complex materials and crystal systems, thereby creating a significant effect that will revolutionize materials development methods.

Among various crystal defects, we focus on GBs and dislocations as essential crystal defects to control macroscopic properties by microscopic distributions. GBs could act as the source of the generation of dislocations^[26–29] to deteriorate macroscopic properties and device performance. As a quantitative model for the dislocation density, the Alexander-Haasen (AH) model^[30] was

developed to describe the multiplication of the dislocations in isotropic material. An extension of the AH model to multiple slip systems is known as the Haasen-Alexander-Sumino (HAS) model,^[31] which successfully addressed multi-axial stress distributions in Si^[32,33] and various semiconductors.^[34] For example, numerical simulation of the stress pattern based on the 3D HAS model explained the dislocation distribution in a quasi-monocrystalline Si ingot grown by directional solidification.^[35] According to the calculation, the dislocation density increases in the early stage of the cooling process after the completion of the crystal growth, which suggests that a large number of dislocations are introduced to relax the thermal stress caused by cooling. On the other hand, in multicrystalline material, the anisotropic elastic constants depending on the crystal orientation should be appropriately treated to obtain the distributions of stress and dislocations. Takahashi et al. carried out 3D finite element stress analysis in a virtual cylindrical Si crystal to contain a single GB by systematically changing the relative orientation,^[36] and revealed that the shear stress can be concentrated around the GB owing to the discontinuous change in the elastic constant. Importantly, the shear stress can be localized at one specific crystal grain, which could explain the nonuniform distribution of dislocations observed in a Si ingot grown using a seed crystal with artificial GBs.^[29,37] It is also proposed that dislocation generation could be assisted by the concentration of thermal stresses introduced by singularities in GBs such as steps and triple junctions.^[28,37–39] However, the generation mechanism has not been clarified at an atomistic level.

In this paper, we report on the integration of experimental, theoretical, computational, and data sciences in multiscale cyber and physical spaces, including research foundations developed in the project such as 3D visualization of dislocation clusters in mc-Si ingot,^[24] prediction of crystal orientation from optical images using machine learning models,^[40,41] crystal growth simulation,^[42] finite element analysis considering anisotropy of elastic constants, observation using electron microscopes, and ab initio calculations, and so on. Integration of these analytical methods made us construct a realistic 3D model of mc-Si and study phenomena that have been difficult to approach from new perspectives, such as dislocation generation in complex multicrystalline materials. As a result, we were able to clarify that the formation of nanofacet structures associated with GB bending is one of the universal origins of dislocation generation.

2. Results and Discussion

Figure 1 shows the overall picture of our methodology. By integrating multiscale experiments, image processing, machine learning and simulations, we explore the dislocation cluster generation and multiplication mechanism by linking microscopic stress analysis during crystal growth on a realistic 3D multicrystalline model and nanoscopic structural analysis. As a macro-scale experiment, we started with the growth of mc-Si ingots and prepared a large amount of Si wafers. PL images containing information on the spatial distribution of crystal defects, mainly composed of dislocation clusters,^[24] were collected from the wafers. Then, optical images of the wafer surfaces were collected with white-light illumination. The reflection characteristics depending on the crystal orientation permitted the grain segmentation,

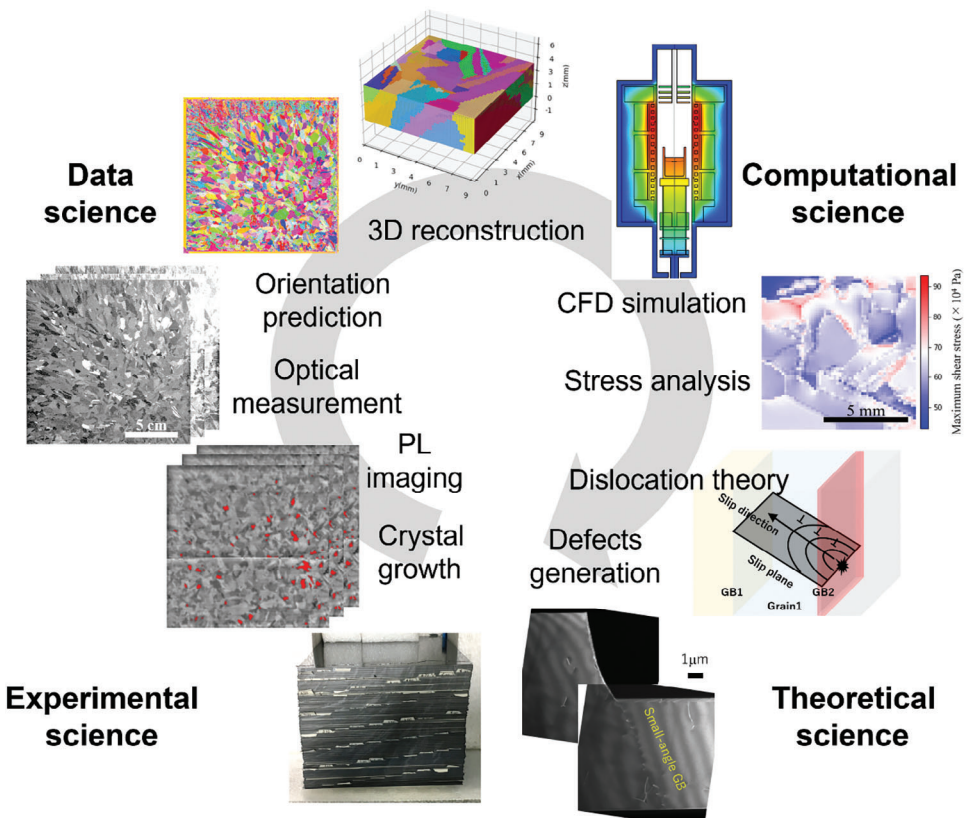


Figure 1. Integration method of various data developed in this study. Mc-Si ingots were fabricated and various imaging techniques were applied to the cut-out wafers. Then, the 3D mc-Si structure was reconstructed by applying image processing to the obtained optical images. The stresses inside the ingot during crystal growth were analyzed from the simulations, and the theory of dislocation cluster generation was discussed by comparing the calculated results with the experimental results.

and prediction of the crystal orientation by the originally developed machine learning model.^[40,41] 3D reconstruction of the multicrystalline microstructure with crystal orientation and the distribution of dislocation clusters were performed using data from several consecutive wafers. Finally, stress analysis was performed at a micro-scale under realistic crystal growth conditions using the 3D reconstructed mc-Si model. We can then identify the dislocation sources in the multi-indexed 3D model; i.e., the GB segments under high shear stresses that emit a number of dislocations. The mechanism of dislocation generation at the extracted GB segments was clarified at a nano-scale by transmission electron microscopy (TEM) and scanning TEM (STEM) assisted by ab initio calculations.

We used 728 of 156 mm × 156 mm × 0.18 mm wafers sliced from a high-performance mc-Si ingot. PL images of the as-sliced wafers were processed to visualize the dislocation clusters (see Experimental Section for the details).^[24] By 3D reconstruction using the processed PL images, we could successfully visualize the generation and propagation of dislocation clusters in the ingots, and we could identify where dislocation clusters generate. In order to obtain 3D mc-Si model with a dislocation source, we selected 13 consecutive wafers in which a dislocation cluster generates and propagates. Figure 2 summarizes 3D reconstruction of a mc-Si model. For each wafer, 36 optical images were taken with the collimated white-light incident from 36 azimuths, and

the outline of the GBs was obtained by image processing (see Experimental Section for the details). As shown in Figure 2a, as well as in the squared area of 10 mm × 10 mm in Figure S1c (Supporting Information), we could successfully identify the grain in which a dislocation cluster generates, by 3D reconstruction using the processed PL and optical images. The shape of dislocation clusters elongated along the growth direction, as previously reported,^[24,25,43] suggesting that they were generated and enlarged just below the solid-liquid interface.

The squared area of 10 mm × 10 mm near the dislocation source was cut out from the 13 wafers, and they were examined more in-depth by high-resolution PL and optical processing (see Experimental Section for the details). PL images were obtained with a high spatial resolution, as shown in Figure S2 (Supporting Information). 36 optical images were taken with 36 azimuths, and each pixel in each image was labeled to determine GBs as the border of the different labels (Figure 2b, right). Furthermore, by stacking these labeled images in the direction of crystal growth, we performed 3D grain segmentation (Figure 2c, left). Each grain was given the crystal orientations at representative points obtained from the orientation prediction method described below as rotations of the elastic tensor (see Experimental Section for the details).^[40,41] The grains arrangement and crystal orientation in the mc-Si structure were successfully reconstructed as in Figure 2c, right, and in Figure S3 (Supporting

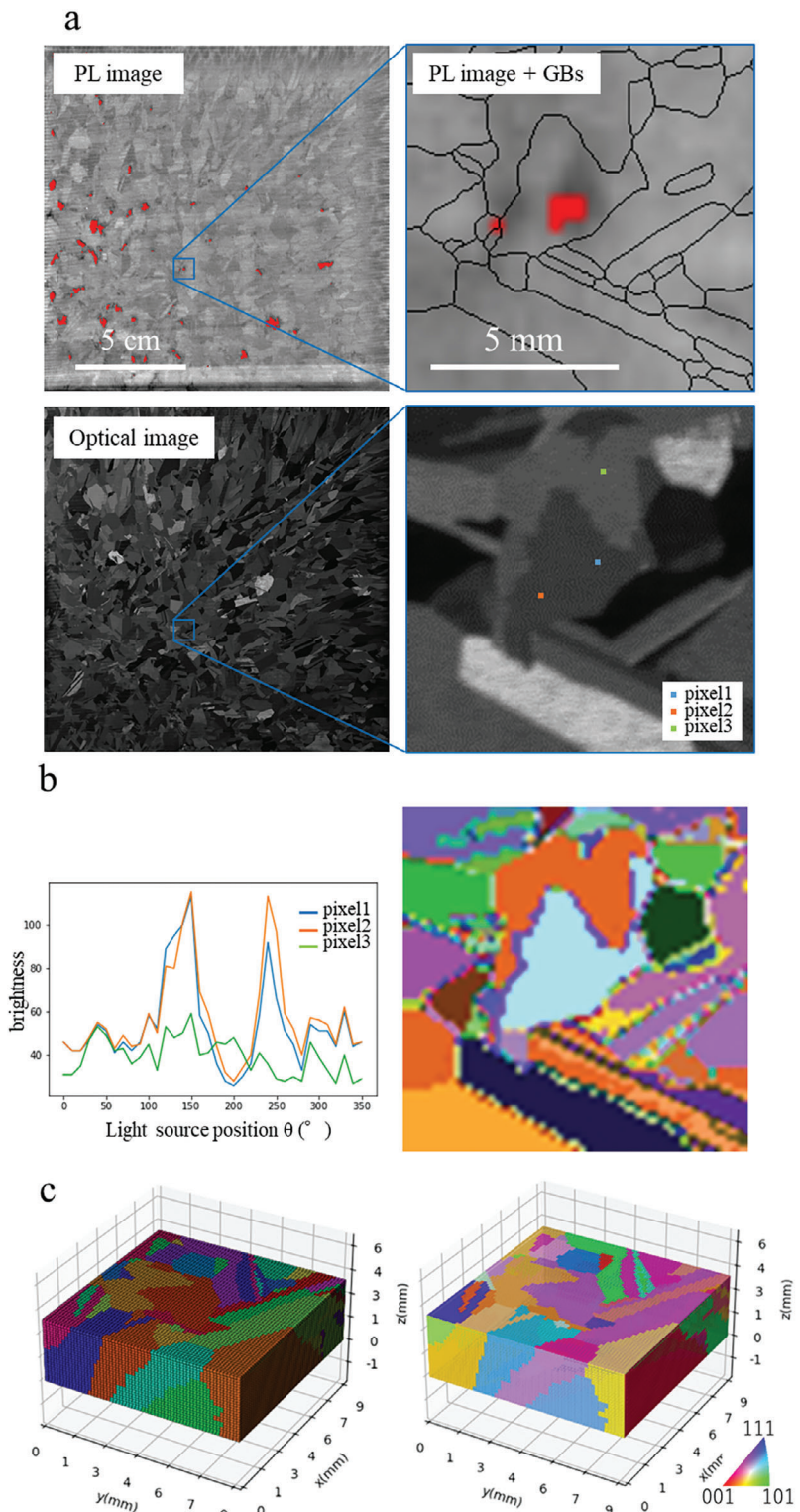


Figure 2. Imaging results of high-performance mc-Si wafers and grain segmentation using reflection characteristics. a) The images are (upper) PL and (lower) optical images of (left) the entire wafer and (right) the area near the dislocation cluster generation point. PL images show dislocation clusters highlighted in red by image processing. b) 36-channel reflection vectors at three representative points and grain segmentation results by Mean Shift Clustering using these reflection properties. The left graph shows that pixel1 and pixel2 have similar reflection properties because they belong to the same grain, while pixel3 has different reflection properties because it belongs to a different grain. c) Left, each grain was randomly colored in the modeling region reconstructed in 3D. Right, each grain was given the orientation of a representative point obtained from the crystal orientation prediction and colored to represent crystal orientations.

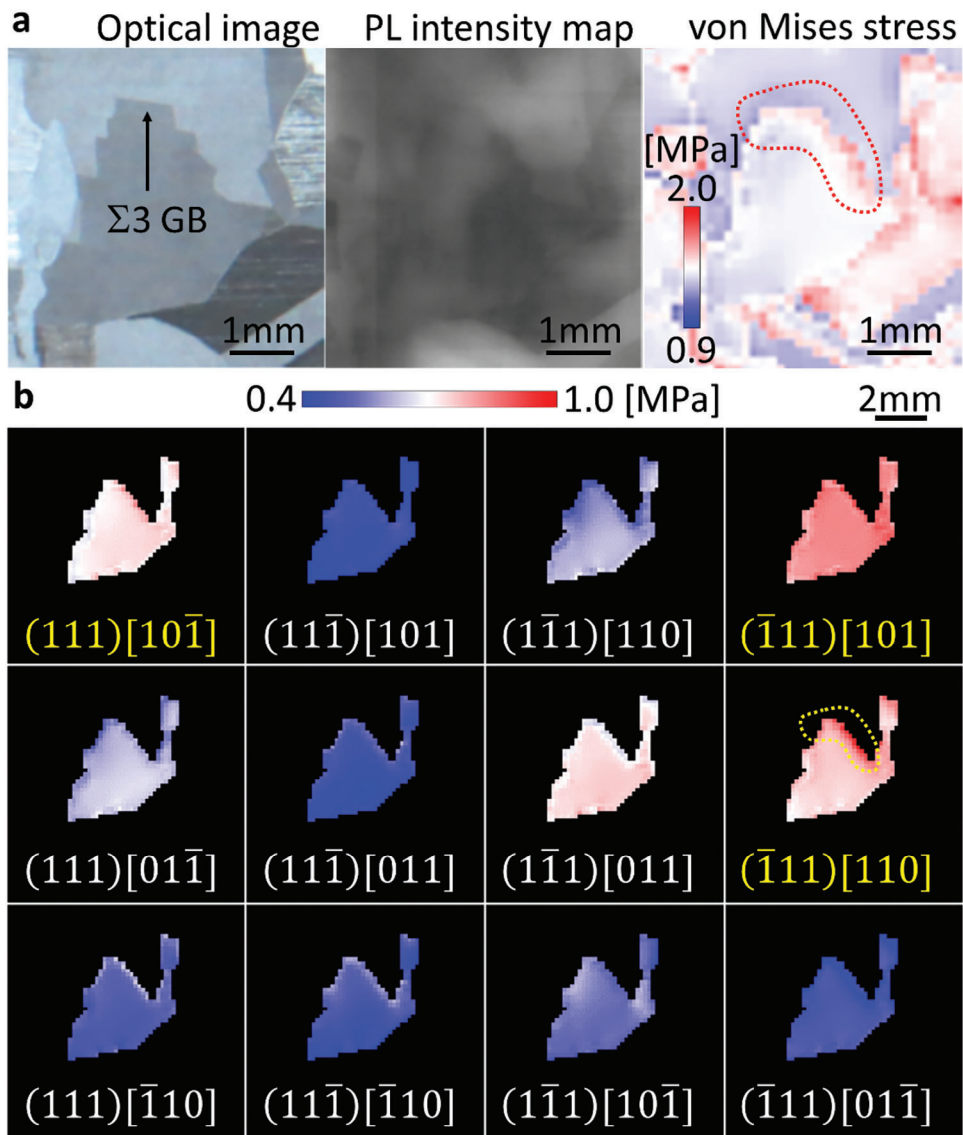


Figure 3. Stress analysis of $\Sigma 3$ grain boundary acting as dislocation sources. a) (left) Optical and (middle) PL images of a grain in which dislocation clusters are generated, and (right) 2D distribution of the von Mises stress in the grain. b) 2D distribution of shear stresses along 12 slip systems consisting of combinations of $\{111\}$ planes and $<110>$ directions. Those stresses are estimated when the grain is just below the solid-liquid interface.

Information). As a result, we could reconstruct the realistic multi-indexed 3D mc-Si model including GB crystallography and dislocation cluster generation point, with the size of $10 \text{ mm} \times 10 \text{ mm} \times 3.6 \text{ mm}$ within a large ingot of $156 \text{ mm} \times 156 \text{ mm} \times 218 \text{ mm}$.

Finite element stress calculations were performed using the reconstructed mc-Si model (see Experimental Section for the details). First, we prepared the 3D model composed of computer aided design (CAD) data of $61 \times 61 \times 13$ parallelepiped elements using the 3D label image shown in Figure 2c, and each grain in the model was given an elasticity matrix calculated from the elastic constants. We then obtained load boundary conditions referring to the stress and temperature distribution just below the solid-liquid interface by using a computational fluid dynamics (CFD) simulation of the directional solidification of a Si ingot. It was expected that compressive stresses of $\sigma_x = -1.71 \text{ MPa}$,

$\sigma_y = -1.50 \text{ MPa}$, $\sigma_z = -0.23 \text{ MPa}$ were applied to each surface of the model, and a temperature gradient from $T_{\text{top}} = 1411.85 \text{ }^\circ\text{C}$ to $T_{\text{bottom}} = 1408.35 \text{ }^\circ\text{C}$ was applied to each node of the model. From the analysis results under the load boundary conditions, we could estimate the 3D distribution of the von Mises stress (or the equivalent stress) in the model as in Figure S5 (Supporting Information). It is seen that the stress is concentrated near the GBs, caused by the discontinuous change in the elastic constant reflecting the different crystal orientations.^[36] The maximum and minimum values are 2.0 and 0.9 MPa, respectively, and the stress concentration is also observed at the GBs nearby the sources of dislocation clusters. Figure 3a shows an example of stress concentration along a GB acting as a dislocation source. The absolute values of the concentrated stresses are in the same order as the yield stress in Si near the melting point (10^0 MPa).^[44] It is

an important finding that our analysis at a micro-scale clarifies a stress distribution in a realistic 3D mc-Si model, and the concentration of high stresses, of the order of the yield stress near the melting point, is observed at the GBs nearby the sources of dislocation clusters, as generally believed. Therefore, this analysis is expected to contribute to the understanding of the effect of microscopic stress during crystal growth on the generation of dislocation clusters.

We also calculated the shear stresses along 12 slip systems consisting of combinations of $\{111\}$ planes and $<110>$ directions. Figure 3b shows the mapping of the shear stress along each of the 12 slip systems, focusing on the GB shown in Figure 3a, at which the dislocation cluster would be generated. The maximum and minimum values are 1.0 and 0.4 MPa, respectively. It is seen that high shear stresses on the three slip systems, $(111)[10\bar{1}]$, $(\bar{1}11)[10\bar{1}]$, and $(111)[110]$, are concentrated along the GB, and dislocations are actually generated in the slip systems, as we demonstrate below. We can predict the nature of dislocations generated from the GB, such as the slip planes and Burgers vectors, by using the multi-indexed 3D model.

Even when examining the structural properties in the reconstructed 3D mc-Si model, common structural characteristics were not identified among the GBs acting as dislocation source. It was also found that there are GBs where a high shear stress is concentrated but dislocations are hardly generated. In Figure 3a, for example, a single GB was concentrated with a high stress surrounds the upper half of the central grain, as seen in the area enclosed by dotted curve, but most dislocations were generated from the GB segment on the right side of the grain. We therefore extracted small foils from the right-side segment by SEM-FIB processing, and their microstructure was examined by TEM and STEM (see Experimental Section for the details). As shown in Figure 4, TEM revealed three kinds of dislocations with the Burgers vectors parallel to $[10\bar{1}]$, $[10\bar{1}]$, and $[110]$. All the dislocations would be generated in the slip systems of $(111)[10\bar{1}]$, $(\bar{1}11)[10\bar{1}]$, and $(111)[110]$, in which high shear stresses at the GB segment were predicted in Figure 3b. Also, the highest shear stress of 1 MPa was expected on the $(\bar{1}11)[110]$ slip system along the GB segment, and a number of dislocations with the Burgers vector parallel to $[110]$ were generated, forming arrays of dislocations (i.e., so called small angle GBs). Occasionally, arrays of dislocations with the Burgers vector parallel to $[10\bar{1}]$ were also formed (Figure S7 in Supporting Information), presumably in the $(111)[10\bar{1}]$ slip system in which the second-highest shear stress was predicted along the GB segment. These results clearly indicate that dislocations are generated at GBs where high shear stresses are concentrated, i.e., stress concentration at GBs is the trigger for dislocation generation. Multiple 3D visualization assisted by machine learning, including GB crystallography, dislocations, and thermal stresses, has made it easier to extract small GB segments acting as dislocation sources in a large mc-Si ingot, enabling efficient progress in nanoscopic analysis of the dislocation sources.

TEM revealed that few dislocations were generated at flat symmetric GB segments such as $\Sigma 3$ GBs lying on $\{111\}/\{111\}$ and $\{112\}/\{112\}$, and a large amount of dislocations were generated from bent GB segments (e.g., Figure 4a), as previously proposed.^[37] This result is consistent with the fact that, the micro-scale analysis of stress distribution shown in Figure 3a reveals

that few dislocations were generated from the flat GB segment at the top of the grain, but most dislocations were generated from the bent GB segments at the right of the grain. On the other hand, high stresses were concentrated almost equally in both GB segments, suggesting that the bent GB segments had some structural characteristics that contribute to dislocation generation. We found that most of the bent segments had a staircase-like structure, composed of symmetric $\Sigma 3$ GB segments lying on $\{111\}/\{111\}$ and $\{112\}/\{112\}$ (Figure 5). Similar symmetric GB segments are frequently observed in micrometer or larger sizes in various mc-Si and are considered to be stable structures. Actually, their GB energies were estimated to be small; 0.0 J/m² for $\Sigma 3\{111\}/\{111\}$ and 0.346 J/m² for $\Sigma 3\{112\}/\{112\}$ by ab initio calculations (see Experimental Section for the details), as previously reported.^[45,46] This indicates that the GB bends while creating a meso-scale staircase-like structure composed of stable GB segments with low GB energy, so as not to increase the GB energy,^[47] from which dislocations would be generated.

Many dislocations were screw-type immediately after their generation, dissociating into pairs of partial dislocations separated by about 4 nm,^[48] and their expansion directions corresponding to their slip directions were almost parallel to one of the junctions of $\{111\}/\{111\}$ and $\{112\}/\{112\}$ segments, as seen in Figure 6 (also in Figures S7 and S8 in Supporting information). Considering the fact that few dislocations were generated at flat GB segments, the vicinity of the facet junctions would be the main sources for dislocation generation. A black blurred region was observed at the facet junctions by HAADF-STEM (Figure 7a), and it was attributed to a tensile bond strain of more than 2% due to lattice expansion along the facet junctions, based on theoretical calculations.^[49,50] On the other hand, macroscopic tensile and compressive experiments on various crystalline materials have shown that the elastic constants including the stiffness decrease with the -5th power of the lattice constant,^[51] and stiffness would be proportional to the yield stress.^[52] Ab initio calculations attributed the decrease to the reduction of the bond strength between neighboring Si atoms (see Experimental Section for the details); the integrated crystal orbital Hamilton population (iCOHP) of Si crystal, inversely correlated with the strength, increased with increasing the lattice constant of Si (Figure 7b). From these results, it is concluded that the yield stress along the facet junctions would be more than 10% lower than that of perfect Si crystals, which would lead to efficient slip along the facet junctions and the formation of screw dislocations. Dislocations expanding nearly parallel to the facet junctions are generated in the three slip systems under high shear stresses. Dislocation generation from non-flat GBs involving microscopic steps were also observed for $\Sigma 3$,^[53] $\Sigma 9$,^[37] $\Sigma 27$,^[37,54] and random-angle GBs.^[28]

We have also found that asymmetric $\Sigma 3$ GB segments lying on $\{113\}/\{557\}$ were sometimes formed instead of $\Sigma 3\{112\}/\{112\}$ segments. Their GB energy was estimated to be 0.36 J m⁻² by ab initio calculations using the structural model constructed from the STEM data (Figures 8a,b). The estimated value is comparable to the GB energy of 0.346 J m⁻² for $\Sigma 3\{112\}/\{112\}$ GBs, resulting in the formation of the asymmetric GB segments as well as in the aid in the GB bending. A tensile bond strain was clarified at the junctions of $\Sigma 3\{111\}/\{111\}$ and $\Sigma 3\{113\}/\{557\}$ segments, along $<1-10>$

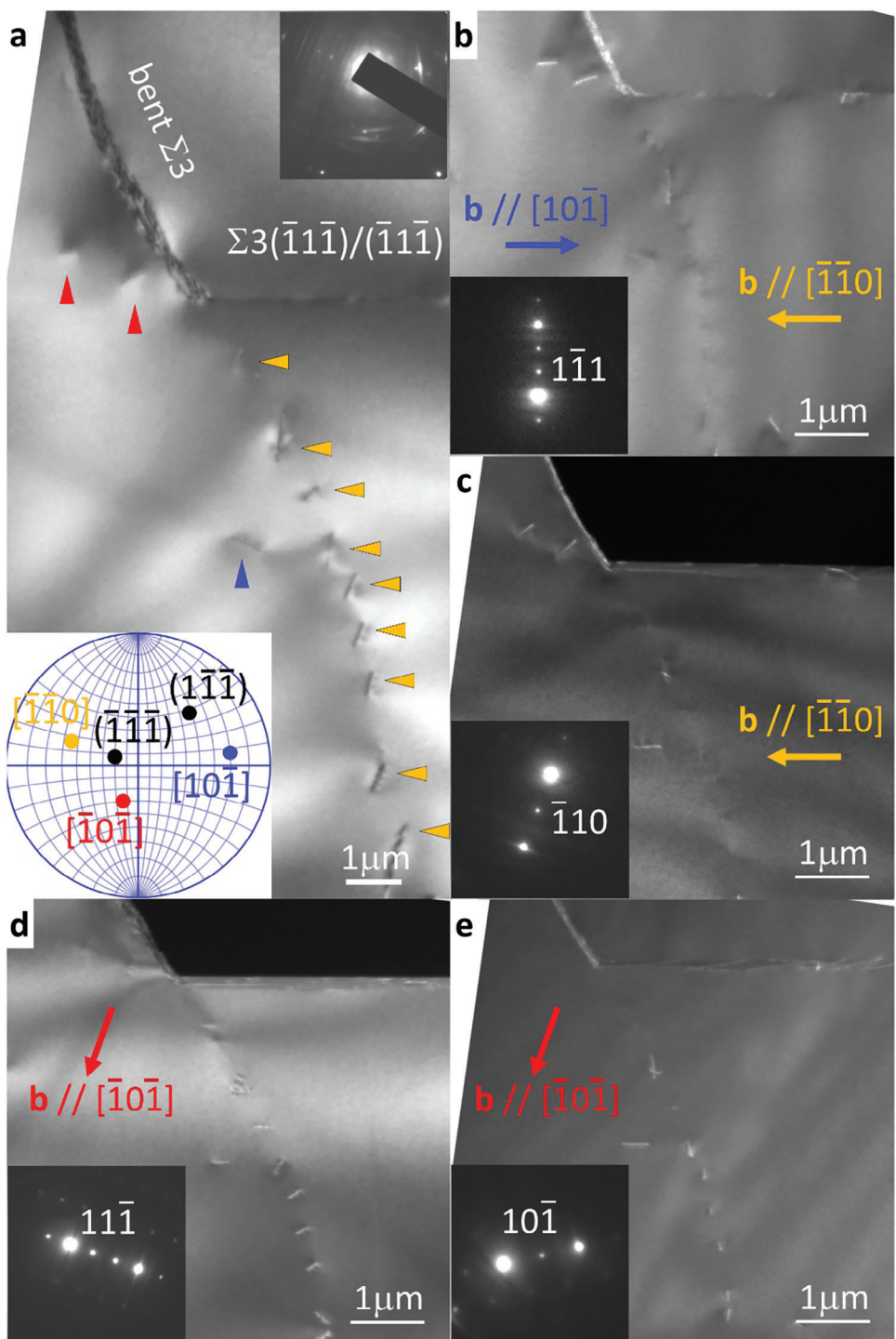


Figure 4. TEM analysis of the Burgers vectors of the dislocations generated at a $\Sigma 3$ GB shown in Figure 3. a) Bright-field TEM by which all the dislocations are visible. b–e) Dislocations are invisible when the Burgers vector is normal to the reflection vector in dark-field TEM. The reflection vectors are b, $[1\bar{1}\bar{1}]$, c, $[\bar{1}10]$, d, $[1\bar{1}\bar{1}]$, and e, $[10\bar{1}]$.

direction (Figure 8c), and it would act as dislocation sources similar to the junctions of $\Sigma 3\{111\}/\{111\}$ and $\Sigma 3\{112\}/\{112\}$ segments. We also found that $\Sigma 3\{113\}/\{557\}$ GBs had a staircase-like structure composed of nano-facets of $\Sigma 3\{111\}/\{111\}$ -like structure, similar to asymmetric $\Sigma 9\{115\}/\{111\}$ GBs,^[55,56] in

which the nano-facet junctions were parallel to $\langle 1-10 \rangle$. Ab initio calculations revealed tensile bond strains of more than 2% along the nano-facet junctions (Figure 6d), presumably due to long $\langle 110 \rangle$ reconstructed bonds,^[57] and it would also act as dislocation sources. Actually, a number of dislocations are

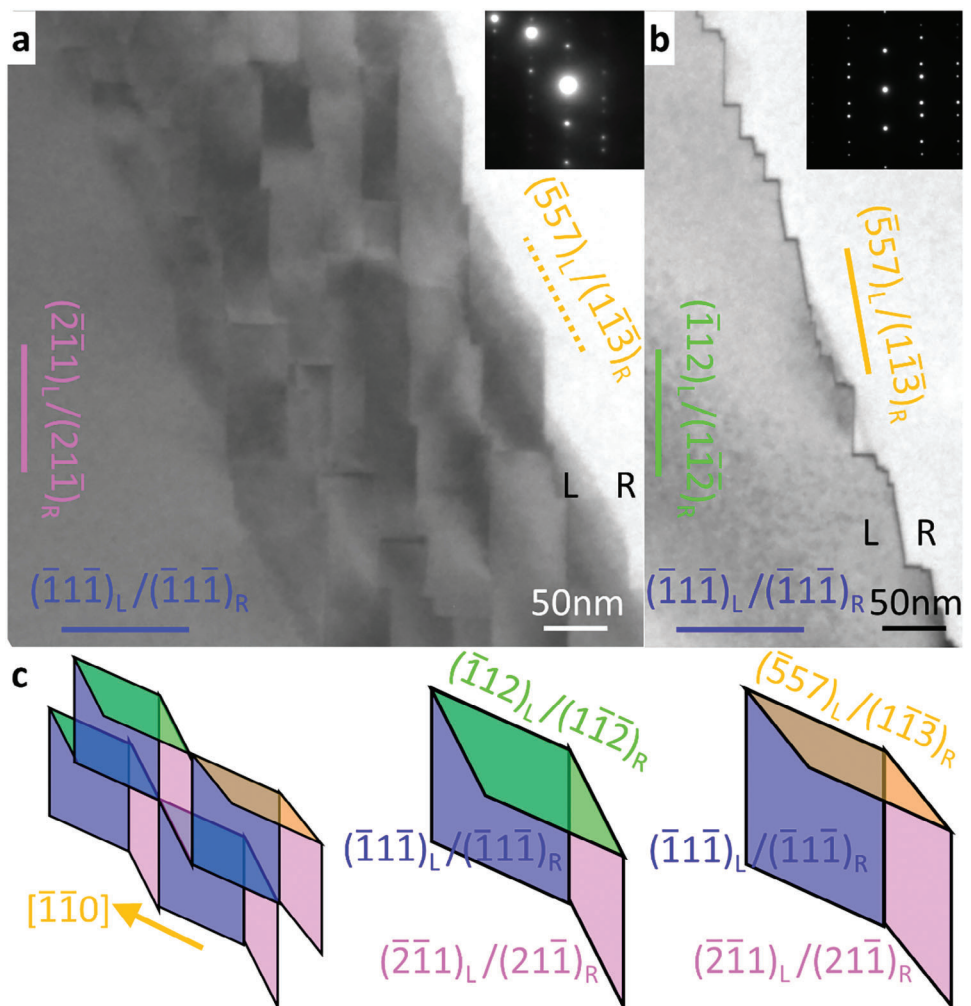


Figure 5. Mesoscopic structural analysis of $\Sigma 3$ GB acting as dislocation sources, using a stereo-TEM (JEOL, JEM-2000EX) operated at 200 kV. The incident directions are a) [011] and b) [110]. c) Staircase-like structures, composed of symmetric segments lying on $\{111\}/\{111\}$ and $\{112\}/\{112\}$ and asymmetric segments lying on $\{113\}/\{557\}$, are formed in bent $\Sigma 3$ grain boundaries.

frequently generated at asymmetric GBs.^[52,53] These results suggest that the formation of facet structures associated with GB bending is one of the universal origins of dislocation generation.

Numerous studies aiming to reduce dislocation density through GB control have advanced from engineering perspectives,^[58–61] and some commercial-scale large mc-Si ingots are being prototyped.^[62,63] We here applied multiscale structural characterization using the machine learning-assisted multi-modal 3D visualization of GB crystallography, dislocations, and thermal stresses. The methodology accelerates the studies and enables us to reveal an aspect of the generation mechanism of dislocations in commercial-scale large Si ingots having a complex multicrystalline structure. The analysis results clearly show that dislocation generation is triggered by thermal stresses at GBs, where the orientation-dependent elastic constants are discontinuous. Also, the methodology enables us to accelerate the analysis of dislocation sources at an atomistic level. We have found that GBs generated during crystal growth do not always propagate as stable symmetric GBs, but sometimes bend while forming a staircase-like structure including asymmetric GB

segments, and these bent GBs can act as dislocation sources via the reduction of the yield stress along the edges of the staircase-like structure. We have reached underlying physical principles in the guidelines to fabricate functional mc-Si ingots with low dislocation density; 1) designing seed crystals that suppress stress generation in consideration of anisotropy of elastic constants, and 2) optimization of crystal growth recipes that lead to suppression and control of thermal stresses, as well as to controlling the direction of GB propagation. The latter guideline is also reasonable from the perspective of electric properties of GBs, since the carrier recombination activity at GBs, often correlated with the segregation ability of impurity atoms at the GBs, is sensitive to the expansion direction of GBs and GB planes.^[50,64]

3. Summary and outlook

This study integrates 3D grain segmentation based on stacking optical and PL images of mc-Si and orientation prediction by machine learning to create a realistic 3D mc-Si model near the

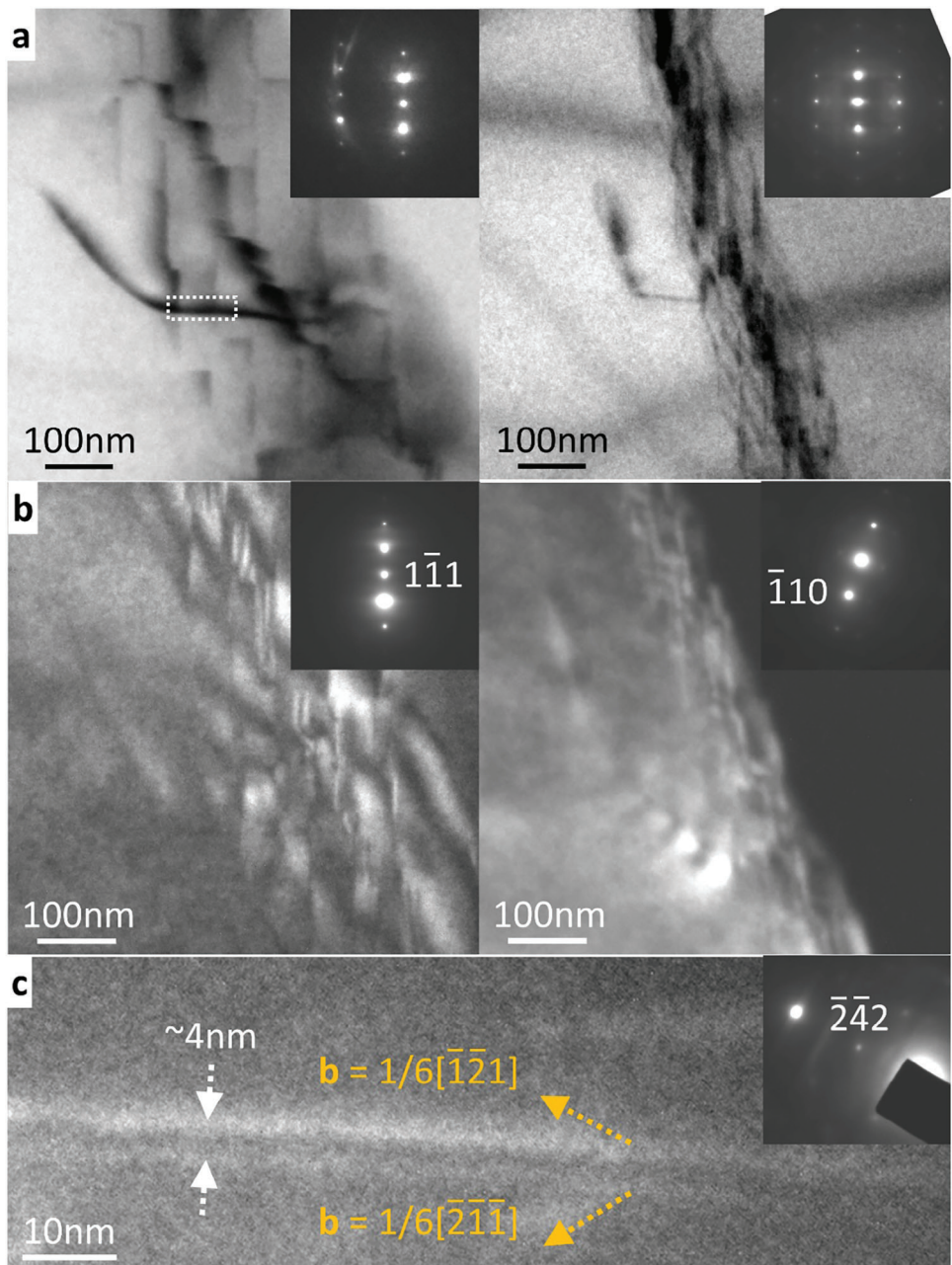


Figure 6. Structural analysis of a dislocation generated at a $\Sigma 3$ GB with staircase-like structures, using a stereo-TEM (JEOL, JEM-2000EX) operated at 200 kV. a) Bright-field stereo-TEM revealed that the dislocation segment near the GB propagates nearly parallel to [110]. b) The Burgers vector of the dislocation is parallel to [110] since the dislocation is almost invisible for the reflection of $[1\bar{1}\bar{1}]$ and $[\bar{1}\bar{1}0]$. c) Weak-beam dark-field TEM revealed that the dislocation is dissociated into a pair of partial dislocations with the Burgers vectors of $1/6[\bar{1}2\bar{1}]$ and $1/6[\bar{2}\bar{1}\bar{1}]$.

point of dislocation cluster generation in a large Si ingot. Furthermore, stress analysis was performed by applying loading boundary conditions to this model with reference to the realistic temperature distribution and internal stress obtained by crystal growth simulation and compared with the observation results to elucidate the dislocation sources. In conclusion, by using the multi-indexed 3D model including GB crystallography, dislocations and thermal stresses, it was found that dislocation clusters in mc-Si are generated at the GB segments at which large shear stresses

are generated during crystal growth, and that the positional relationship between the slip system and GBs is important. Furthermore, multiscale structural analysis of the extracted GB segments acting as dislocation sources was performed by TEM/STEM assisted by SEM-FIB and ab initio calculations. It was found that singularities in the GB segments, i.e., facet structures at nanoscale to micro-scale that would reduce the yield stress, reveal the existence of a dislocation generation mechanism unique to the multicrystalline structure. Further systematic investigation is

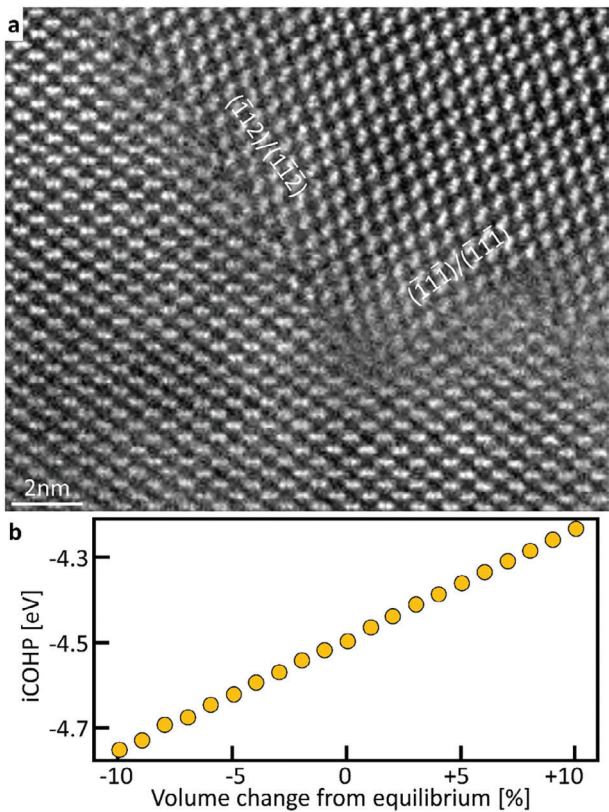


Figure 7. Atomistic structure of dislocation sources organized at Σ_3 GBs examined with a JEOL ARM200F analytical microscope. a) HAADF-STEM of junctions of $\Sigma_3\{111\}/\{111\}$ and $\Sigma_3\{112\}/\{112\}$ GB segments along which a high tensile stress is concentrated. b) The iCOHP of Si crystal, related to the covalent bond strength between neighboring Si atoms, as a function of volume change of Si crystal.

expected to lead to applications to the design of high-quality ingots. In addition, the method used in this study can be applied to many other multicrystalline materials. High crystal defect density is a common problem in multicrystalline materials, and this method will be useful for systematizing universal guidelines for high performance of multicrystalline materials.

4. Experimental Section

Sample Preparation: Four bricks, 156 mm \times 156 mm \times \sim 220 mm in size, were cut out from a high-performance mc-Si ingot grown by the directional solidification method at Kyocera. Each brick was sliced into 728 of 156 mm \times 156 mm \times 180 μm wafers at a slice pitch of 0.3 mm with diamond wires.

PL Imaging to Visualize 3D Distribution of Dislocation Clusters: PL imaging was used to measure the dislocation distribution in mc-Si wafers under two conditions depending on the sample size and purpose. PL images of the as-sliced wafers, 156 mm \times 156 mm \times 180 μm in size, were obtained using a PL measurement system (Hamamatsu Photonics EPL-100s) with a 940 nm laser, and they were processed to visualize the dislocation clusters by smoothing and unsharp-mask filtering with preprocessing (FFT, IFFT, gray level normalization, and thresholding).^[24] On the contrary, for the observation near a dislocation source, a sample of 10 mm \times 10 mm \times 180 μm was cut out nearby the source. It was passivated with quinhydrone methanol for 1 h to suppress surface recombination, and PL images were

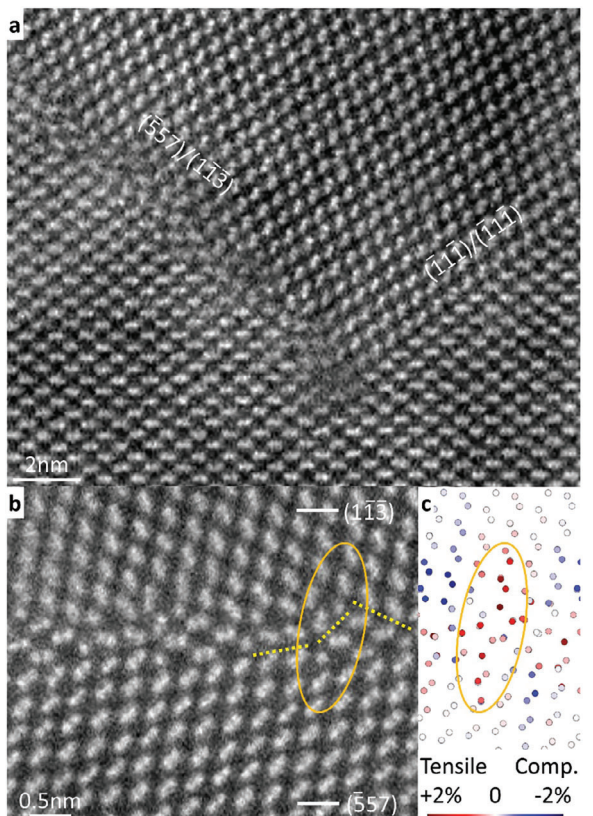


Figure 8. Atomistic structure of dislocation sources organized at Σ_3 GBs examined with a JEOL ARM200F analytical microscope. a) HAADF-STEM of a junction of $\Sigma_3\{111\}/\{111\}$ and $\Sigma_3\{113\}/\{557\}$ GB segments along which a high tensile stress is concentrated. b) Magnified STEM of $\Sigma_3\{113\}/\{557\}$ GB segment. c) 2D distribution of bond strains around the segment obtained by ab initio calculations.

obtained with a high spatial resolution using a laser of 532 nm. In this case, a small area of 2 mm \times 2 mm was stitched together to form a single image due to the limited field of view.

Optical Imaging for 3D Segmentation of GBs: Optical imaging was used to determine the grain and GB distribution in mc-Si wafers under two conditions depending on the sample size and purpose. Before imaging, wafers were etched with an alkaline solution to form a textured structure on the surfaces, i.e., pyramidal projections surrounded by $\{111\}$ facets, which depend on the crystal orientation. Optical images were obtained using the original equipment. In the system, the position of the white collimated light source can be rotated in the azimuthal and elevation directions around the sample stage to change the direction of the incident light, so that the differences in reflection properties due to surface morphology among the grains can be detected. The reflected light from the sample is measured by the imaging photometer placed directly above the stage. To detect the grains and GBs, 36 optical images for each wafer were taken with incident light from 36 azimuths (10° steps) at an elevation angle of 60°, as exemplified in Figure S1a (Supporting Information). By changing the position of the light source when capturing optical images, the grains in the wafer had reflection characteristics that depend on the crystal orientation.

To depict GBs image across the entire 156 \times 156 mm² wafer, Canny edge detection algorithm was applied to each of the 36 optical images, and the edges of each image were overlaid onto a single image.^[65] This image contained linear features (GBs) and punctate patterns (artefacts), so we performed a pixel-wise segmentation with manual annotation to extract only GBs using Trainable Weka Segmentation, a ImageJ-Fiji plugin, which

provides simple GUI for executing both annotation and segmentation^[66] as in Figure S1b (Supporting Information).

For the observation near a dislocation source, a $10 \times 10 \text{ mm}^2$ region was selected, and each set of 36 optical images in 13 wafers adjacent the vertical direction, corresponding to approximately 3.6 mm in the height of the ingot, was labeled into individual grains by mean-shift clustering on 36-dimensional values of reflection intensity vectors.^[67] Small regions derived from noisy values were removed and dilation processing were applied to the valid regions. Then, fine noises were removed manually. The pixels classified to the same label were consolidated into a grain to construct a 3D multicrystalline model.

Machine Learning to Predict Crystal Orientations: Crystal orientation was predicted with optical imaging data assisted by machine learning. The 72×2 signal matrix extracted from pixel values in the 144 optical images (obtained with 72 azimuths (5° steps) at an elevation angle of 45° and 60° by the above-mentioned instrument) was utilized as an input to the machine learning model. The estimation model consisted of a Long Short-Term Memory (LSTM) layer and three fully connected layers, and the model was trained using the crystal orientations in the four wafers, which were obtained by X-ray diffraction-based Laue scanner method as the ground truth.^[40,41] The crystal orientations of 4 795 grains in three substrates were divided into 3 838 training and 960 validation data, and 1 552 in the other substrate were used for test data. The training data were expanded by a factor of 144, resulting in a total of 551 520 data, by symmetric operations on signal matrix and crystal orientations. The estimation error on the test data exhibited a median of 2.4° , an average of 3.8° , and a 95th percentile of 8.4° .

Finite Element Analysis for 3D Stress Evaluation: 3D distribution of thermal stresses was evaluated when a dislocation cluster was generated by finite element stress calculations using the reconstructed mc-Si model shown in Figure 2c, right.

First, the 3D label image in Figure 2c was converted into computer aided design (CAD) data of $61 \times 61 \times 13$ parallelepiped elements via DREAM.3D, an open-source software for the 3D reconstruction of multi- and polycrystalline microstructures,^[68] and this was used as the geometry of the model. Each grain in the model was given an elastic modulus rotated as a function of the crystal orientation. The unrotated elastic modulus in the Si crystal coordinate for the simulation at high temperature just below the melting point was calculated from the temperature dependent Young's moduli E_{100} , E_{110} , and E_{111} of Si, since the elastic tensor could be derived from three independent constants due to the symmetry of the diamond structure. The temperature dependence of Young's moduli was expressed by the semi-empirical Wachtmann equation^[69]:

$$E_{ijk}(T) = E_{0,ijk} - \Omega_{ijk} T \exp\left(-\frac{T_{W,ijk}}{T}\right) \quad (1)$$

where the constants $E_{0,ijk}$, Ω_{ijk} , and $T_{W,ijk}$ were adopted from the values presented in the paper.^[70] By solving the system of the Equations 4–6 in Ref. [69], the relations between Young's moduli and elastic compliance matrix s_{ij} in Voigt notation were obtained as:

$$s_{11} = \frac{1}{E_{100}} \quad (2)$$

$$s_{12} = \frac{2E_{100} - E_{110} - \sqrt{A}}{2E_{100}E_{110}} \quad (3)$$

$$s_{44} = \frac{2E_{100} - E_{110} + \sqrt{A}}{E_{100}E_{110}} \quad (4)$$

in which $A = 4E_{100}^2 - 8E_{100}E_{110} + 5E_{110}^2$. The other elements in the 6×6 elastic compliance matrix in Voigt notation were $s_{11} = s_{22} = s_{33}$, $s_{12} = s_{13} = s_{23}$, and $s_{44} = s_{55} = s_{66}$ due to the cubic symmetry, and the residual elements were zero. The elastic modulus c_{ij} in Voigt notation could be obtained as the inverse matrix of s_{ij} . The calculated values of the elastic

Table 1. Slip system of Si crystal.

| Slip plane | Slip direction 1 | Slip direction 2 | Slip direction 3 |
|------------|------------------|------------------|------------------|
| (111) | [10̄1] | [01̄1] | [̄110] |
| (1̄1̄1) | [101] | [011] | [̄110] |
| (1̄1̄1) | [110] | [011] | [10̄1] |
| (̄11) | [101] | [110] | [011̄] |

modulus matrix at 1410°C were $c_{11} = 137.7 \text{ GPa}$, $c_{12} = 49.00 \text{ GPa}$, and $c_{44} = 67.62 \text{ GPa}$. The $3 \times 3 \times 3 \times 3$ fourth-order tensor C_{ijkl} of the elastic modulus was achieved by mapping the matrix elements to the corresponding indices in Voigt notation. The tensor could be rotated by the 3×3 rotation matrix R_{ij} , representing the crystal orientation of each grain as:

$$C'_{ijkl} = \sum_{p,q,r,s} R_{ip} R_{jq} R_{kr} R_{ls} C_{pqrs} \quad (5)$$

Then, stress calculations on the 3D model with elastic moduli was performed with a finite element solver with stress, structural, and thermal simulation capabilities, Ansys® Mechanical, Release 2021 R1, ANSYS inc. Load boundary conditions referring to the stress and temperature distribution just below the solid-liquid interface were obtained by a CFD simulation denoted in the next section. It was expected that compressive stresses of $\sigma_x = -1.71 \text{ MPa}$, $\sigma_y = -1.50 \text{ MPa}$, $\sigma_z = -0.23 \text{ MPa}$ were applied to each surface of the model, and a temperature gradient from $T_{\text{top}} = 1411.85^\circ\text{C}$ to $T_{\text{bottom}} = 1408.35^\circ\text{C}$ was applied in the z direction of the model. The elastic modulus of each element was calculated as functions of the given crystal orientation and the temperature. In addition to the load boundary condition, constraints were applied to the three vertices of the bottom plane of the model to avoid the model rotation.

The results of the calculations were given to each node in the form of a stress tensor. The shear stresses along 12 slip systems consisting of combinations of {111} planes and <110> directions were calculated by the following equation.

$$\tau = n \cdot \sigma \cdot s = [n_x \ n_y \ n_z] \begin{bmatrix} \sigma_x & \tau_{xy} & \tau_{xz} \\ \tau_{xy} & \sigma_y & \tau_{yz} \\ \tau_{xz} & \tau_{yz} & \sigma_z \end{bmatrix} \begin{bmatrix} s_x \\ s_y \\ s_z \end{bmatrix} \quad (6)$$

where n , σ , and s are the normal vector of a slip plane, the stress tensor, and the unit vector in the slip direction (Table 1).

CFD Simulation of Directional Solidification of a Si Ingot: The load boundary conditions referring to the stress and temperature distribution for the finite element stress calculations were determined based on the results of the CFD simulation of the directional solidification of a Si ingot. The CFD simulation modeled the actual vertical Bridgeman-type crystal growth furnace consisting of a stainless chamber, three-zone graphite heaters, graphite thermal insulators, a silica crucible, and its susceptor in 2D axis symmetry as shown in Figure S4. Each part was differentiated with sufficiently small size meshes, e.g., $1 \text{ mm} \times 1 \text{ mm}$ element size for the Si melt. Unsteady state simulation was performed following the sequential program for furnace control. The heater powers were controlled to fit the temperature at the monitoring point with the programmed temperature as in the case of the real furnace control. The temperature distribution in the ingot was calculated by solving the coupling thermal transport simulations of fluid dynamics of Si melt in the crucible and Ar gas in the chamber, thermal diffusion, and radiation. The boundary condition stress at the periphery of the calculation volume of the multicrystalline stress analysis was calculated using the temperature distribution and elastic constant for a single crystalline Si. CGSim (STR inc.) was used for these crystal growth and stress analysis simulations. The detail of the crystal growth furnace model and simulation is described in Ref. [42].

TEM/STEM Imaging for Structural Characterization of GBs and Dislocations: Mesoscopic morphology of $\Sigma 3$ GB segments and dislocations, as

well as the Burgers vectors of the dislocations, were examined using a stereo-TEM (JEOL, JEM-2000EX) operated at 200 kV. Thin foils for TEM, about $30\text{ }\mu\text{m} \times 30\text{ }\mu\text{m} \times 0.5\text{ }\mu\text{m}$ in size, were cut from a wafer so that the foil surfaces were parallel to the wafer, by conventional focused ion beam (FIB) processing using a FIB system (FEI, Helios NanoLab600i) with 2–30 kV Ga ions. The Burgers vector of a dislocation was determined by finding the reflection in which the dislocation was invisible if $\mathbf{g} \cdot \mathbf{b} = 0$.^[71] Thin foils with a $\Sigma 3$ GB for HAADF-STEM, about $10\text{ }\mu\text{m} \times 10\text{ }\mu\text{m} \times 0.2\text{ }\mu\text{m}$ in size, were cut from a wafer so that an $<110>$ tilt axis of the GB was normal to the foil surfaces, by a micro-sampling technique using FIB combined with scanning electron microscopy (SEM) and electron back-scattered diffraction (EBSD) (e.g., Figure S6 in Supporting Information). Atomic arrangement at the GB was examined by HAADF-STEM with a JEOL ARM200F analytical microscope operated at 200 kV. The spatial resolution was 0.1 nm.

Ab Initio Calculations to Assess GB Structures with Bond Strains: The atomistic structure of GBs was examined by performing ab initio calculations. Supercells with a $\Sigma 3\{111\}/\{111\}$ GB (consisting of 48 Si atoms, whose cell volume was $3.77 \times 0.67 \times 0.38\text{ nm}^3$), $\Sigma 3\{112\}/\{112\}$ GB (80 Si atoms, $2.40 \times 0.94 \times 0.77\text{ nm}^3$), and $\Sigma 3\{113\}/\{557\}$ GB (382 Si atoms, $1.91 \times 5.00 \times 0.38\text{ nm}^3$) were constructed by using the HAADF-STEM data. Density-functional-theory (DFT) calculations were performed using the projector augmented wave (PAW) method^[72,73] implemented in the VASP code.^[74,75] The exchange-correlation energy was calculated using a revised version of the generalized gradient approximation formulated by Perdew, Burke and Ernzerhof (GGA-PBEsol).^[76] An energy cutoff of 500 eV was used for the plane-wave basis set, and $8 \times 8 \times 8$ meshes were used in k -point sampling for a conventional cubic cell. The convergence criterion for total energy was set to 10^{-6} eV. The atomic positions were optimized until the force acting on each atom was less than $10^{-2}\text{ eV } \text{\AA}^{-1}$.

In order to evaluate the bond strength between neighboring Si atoms, crystal orbital Hamilton population (COHP) analysis was employed.^[77] The COHP analysis is a technique for partitioning the band-structure energy into bonding, nonbonding, and antibonding contributions using localized atomic basis sets, describing as a hopping-weighted density-of-states between a pair of adjacent atoms. In analogy to the density of states (DOS), for which the energy integration up to the Fermi energy gives the number of electrons, the energy integration of all COHP for a pair of atoms up to the Fermi energy (iCOHP) can imply the bond strength.^[78] The iCOHP of Si crystal was estimated as a function of volume change of Si crystal, using the LOBSTER code.^[79]

Supporting Information

Supporting Information is available from the Wiley Online Library or from the author.

Acknowledgements

K.Y. and Y.O. contributed equally to this work. This work was partly supported by JST/CREST under Grant No. JPMJCR17J1 (2017-2023) and Nagoya University Research Fund. TEM/STEM specimen fabrication was supported by the GIMRT Program in IMR, Tohoku University, Grant No. 202211-IRKMA-0407, and STEM analysis was supported by the NJRC Program in SANKEN, Osaka University, Grant No. 20221182.

Conflict of Interest

The authors declare no conflict of interest.

Data Availability Statement

The data that support the findings of this study are available from the corresponding author upon reasonable request.

Keywords

ab initio calculation, computational fluid dynamics simulation, dislocation clusters, finite element stress analysis, grain boundaries, machine learning, multiscale structural characterizations

Received: August 23, 2023

Revised: November 19, 2023

Published online: December 10, 2023

- [1] T. Watanabe, *J. Mater. Sci.* **2011**, *46*, 4095.
- [2] Y. Zhang, T. T. Zuo, Z. Tang, M. C. Gao, K. A. Dahmen, P. K. Liaw, Z. P. Lu, *Prog. Mater. Sci.* **2014**, *61*, 1.
- [3] R. Z. Valiev, R. K. Islamgaliev, I. V. Alexandrov, *Bulk Nanostructured Materials from Severe Plastic Deformation*, **2000**.
- [4] T. D. Ngo, A. Kashani, G. Imbalzano, K. T. Q. Nguyen, D. Hui, *Composites, Part B* **2018**, *143*, 172.
- [5] C. W. Lan, *Handb. Photovolt. Silicon* **2019**, 175.
- [6] A. R. Krause, P. R. Cantwell, C. J. Marvel, C. Compson, J. M. Rickman, M. P. Harmer, *J. Am. Ceram. Soc.* **2018**, *102*, 778.
- [7] A. Agrawal, A. Choudhary, *APL Mater.* **2016**, *4*, 053208.
- [8] J. M. Rickman, H. M. Chan, M. P. Harmer, J. A. Smeltzer, C. J. Marvel, A. Roy, G. Balasubramanian, *Nat. Commun.* **2019**, *10*, 2618.
- [9] Z. Wang, Z. Sun, H. Yin, X. Liu, J. Wang, H. Zhao, C. H. Pang, T. Wu, S. Li, Z. Yin, X.-F. Yu, *Adv. Mater.* **2022**, *34*, 2104113.
- [10] R. Feng, C. Zhang, M. C. Gao, Z. Pei, F. Zhang, Y. Chen, D. Ma, K. An, J. D. Poplawsky, L. Ouyang, Y. Ren, J. A. Hawk, M. Widom, P. K. Liaw, *Nat. Commun.* **2021**, *12*, 6.
- [11] Y. Iwasaki, I. Takeuchi, V. Stanev, A. G. Kusne, M. Ishida, A. Kirihara, K. Ihara, R. Sawada, K. Terashima, H. Someya, K.-I. Uchida, E. Saitoh, S. Yorozu, *Sci. Rep.* **2019**, *9*, 2751.
- [12] Y. Wu, J. Guo, R. Sun, J. Min, *npj Comput. Mater.* **2020**, *6*, 120.
- [13] M. Minkowski, L. Laurson, *Sci. Rep.* **2023**, *13*, 13977.
- [14] X. Zheng, T. Sun, J. Zhou, R. Zhang, P. Ming, *Materials* **2022**, *15*, 1996.
- [15] S. L. Thomas, K. Chen, J. Han, P. K. Purohit, D. J. Srolovitz, *Nat. Commun.* **2017**, *8*, 1764.
- [16] G. Agarwal, R. R. Valisetty, R. R. Namburu, A. M. Rajendran, A. M. Dongare, *Sci. Rep.* **2017**, *7*, 12376.
- [17] M. Pinz, G. Weber, J. C. Stinville, T. Pollock, S. Ghosh, *npj Comput. Mater.* **2022**, *8*, 39.
- [18] H. Chan, M. Cherukara, T. D. Loeffler, B. Narayanan, S. K. R. S. Sankaranarayanan, *npj Comput. Mater.* **2020**, *6*, 1.
- [19] T. Trupke, R. A. Bardos, M. C. Schubert, W. Warta, *Appl. Phys. Lett.* **2006**, *89*, 044107.
- [20] M. Demant, P. Virtue, A. Kovvali, S. X. Yu, S. Rein, *IEEE J. Photovolt.* **2019**, *9*, 1073.
- [21] M. Demant, P. Virtue, A. Kovvali, S. X. Yu, S. Rein, *IEEE J. Photovolt.* **2019**, *9*, 1064.
- [22] T. Strauch, M. Demant, P. Krenkel, S. Riepe, S. Rein, *J. Cryst. Growth* **2016**, *454*, 147.
- [23] T. Strauch, M. Demant, P. Krenkel, S. Riepe, S. Rein, in *EU PVSEC 2017*, **2017**, pp. 313–317.
- [24] Y. Hayama, T. Matsumoto, T. Muramatsu, K. Kutsukake, H. Kudo, N. Usami, *Sol. Energy Mater. Sol. Cells* **2019**, *189*, 239.
- [25] J. Schönauer, M. Demant, T. Trötschler, A. S. Kovvali, H. Schremmer, P. Krenkel, S. Riepe, S. Rein, in *EU PVSEC 2020*, **2020**, pp. 113–120.
- [26] J. Reiser, A. Hartmaier, *Sci. Rep.* **2020**, *10*, 2739.
- [27] J. Li, G. M. Pharr, C. Kirchlechner, *J. Mater. Res.* **2021**, *36*, 2037.
- [28] Y. Ohno, K. Tajima, K. Kutsukake, N. Usami, *Appl. Phys. Express* **2020**, *13*, 105505.
- [29] I. Takahashi, N. Usami, K. Kutsukake, G. Stokkan, K. Morishita, K. Nakajima, *J. Cryst. Growth* **2010**, *312*, 897.

- [30] I. T. Alexander, P. Haasen, *Solid State Phys.* **1969**, 22, 27.
- [31] M. Suezawa, K. Sumino, I. Yonenaga, *Phys. Stat. Sol. (a)* **1979**, 51, 217.
- [32] O. W. Dillon, C. T. Tsai, R. J. De Angelis, *J. Appl. Phys.* **1986**, 60, 1784.
- [33] J. Völk, G. Müller, *J. Cryst. Growth* **1989**, 97, 136.
- [34] N. Miyazaki, S. Okuyama, *J. Cryst. Growth* **1998**, 183, 81.
- [35] S. Nakano, B. Gao, K. Jiptner, H. Harada, Y. Miyamura, T. Sekiguchi, M. Fukuzawa, K. Kakimoto, *J. Cryst. Growth* **2017**, 474, 130.
- [36] I. Takahashi, N. Usami, K. Kutsukake, K. Morishita, K. Nakajima, *Jpn. J. Appl. Phys.* **2010**, 49, 04DP01.
- [37] A. Autruffe, V. Stenhammar Hagen, L. Arnborg, M. Di Sabatino, *J. Cryst. Growth* **2015**, 411, 12.
- [38] M. G. Tsoutsouva, T. Riberi - Béridot, G. Regula, G. Reinhart, J. Baruchel, F. Guittoneau, L. Barrallier, N. Mangelinck-Noël, *Acta Mater.* **2016**, 115, 210.
- [39] M. M. Kivambe, T. Ervik, B. Ryningen, G. Stokkan, *J. Appl. Phys.* **2012**, 112, 103528.
- [40] H. Kato, S. Kamibeppu, T. Kojima, T. Matsumoto, H. Kudo, Y. Takeuchi, K. Kutsukake, N. Usami, *IEEJ Trans* **2022**, 17, 1685.
- [41] K. Hara, T. Kojima, K. Kutsukake, H. Kudo, N. Usami, *APL Mach. Learn.* **2023**, 1, 026113.
- [42] X. Liu, Y. Dang, H. Tanaka, Y. Fukuda, K. Kutsukake, T. Kojima, T. Ujihara, N. Usami, *ACS Omega* **2022**, 7, 6665.
- [43] M. G. Tsoutsouva, G. Regula, B. Ryningen, P. E. Vullum, N. Mangelinck-Noël, G. Stokkan, *Acta Mater.* **2021**, 210, 116819.
- [44] I. Yonenaga, *J. Electrochem. Soc.* **1996**, 143, L176.
- [45] R. Maji, E. Luppi, N. Caproni, E. Degoli, *Acta Mater.* **2021**, 204, 116477.
- [46] C. B. Feng, J. L. Nie, X. T. Zu, M. M. Al-Jassim, Y. Yan, *J. Appl. Phys.* **2009**, 106, 113506.
- [47] Y. Fukuda, K. Kutsukake, T. Kojima, N. Usami, *CrystEngComm* **2022**, 24, 1948.
- [48] Y. Ohno, T. Taishi, Y. Tokumoto, I. Yonenaga, *J. Appl. Phys.* **2010**, 108, 073514.
- [49] C. H. Liebscher, A. Stoffers, M. Alam, L. Lymerakis, O. Cojocaru-Mirédin, B. Gault, J. Neugebauer, G. Dehm, C. Scheu, D. Raabe, *Phys. Rev. Lett.* **2018**, 121, 015702.
- [50] Y. Ohno, T. Tamaoka, H. Yoshida, Y. Shimizu, K. Kutsukake, Y. Nagai, N. Usami, *Appl. Phys. Express* **2021**, 14, 011002.
- [51] I. Yonenaga, Y. Ohkubo, M. Deura, K. Kutsukake, Y. Tokumoto, Y. Ohno, A. Yoshikawa, X. Q. Wang, *AIP Adv.* **2015**, 5, 077131.
- [52] R. A. Varin, K. Tangri, *Mater. Sci. Eng.* **1985**, 72, 177.
- [53] V. A. Oliveira, B. Marie, C. Cayron, M. Marinova, M. G. Tsoutsouva, H. C. Sio, T. A. Lafford, J. Baruchel, G. Audit, A. Grenier, T. N. Tran Thi, D. Camel, *Acta Mater.* **2016**, 121, 24.
- [54] B. Ryningen, G. Stokkan, M. Kivambe, T. Ervik, O. Lohne, *Acta Mater.* **2011**, 59, 7703.
- [55] Y. Ohno, K. Inoue, K. Fujiwara, K. Kutsukake, M. Deura, I. Yonenaga, N. Ebisawa, Y. Shimizu, K. Inoue, Y. Nagai, H. Yoshida, S. Takeda, S. Tanaka, M. Kohyama, *Appl. Phys. Lett.* **2017**, 110, 062105.
- [56] A. Stoffers, B. Ziebarth, J. Barthel, O. Cojocaru-Mirédin, C. Elsässer, D. Raabe, *Phys. Rev. Lett.* **2015**, 115, 235502.
- [57] Y. Ohno, J. Ren, S. Tanaka, M. Kohyama, K. Inoue, Y. Shimizu, Y. Nagai, H. Yoshida, *Appl. Phys. Express* **2021**, 14, 041003.
- [58] K. Kutsukake, N. Usami, Y. Ohno, Y. Tokumoto, I. Yonenaga, *IEEE J. Photovolt.* **2014**, 4, 84.
- [59] D. Hu, S. Yuan, L. He, H. Chen, Y. Wan, X. Yu, D. Yang, *Sol. Energy Mater. Sol. Cells* **2015**, 140, 121.
- [60] T. Iwata, I. Takahashi, N. Usami, *Jpn. J. Appl. Phys.* **2017**, 56, 075501.
- [61] F. Zhang, X. Yu, C. Liu, S. Yuan, X. Zhu, Z. Zhang, L. Huang, Q. Lei, D. Hu, D. Yang, *Sol. Energy Mater. Sol. Cells* **2019**, 200, 109985.
- [62] P. Wang, C. Cui, D. Yang, X. Yu, *Sol. RRL* **2020**, 4, 1900486.
- [63] S. Tang, X. Qi, C. Chang, Q. Wang, L. Liu, *J. Cryst. Growth* **2023**, 607, 127109.
- [64] Y. Fukuda, K. Kutsukake, T. Kojima, Y. Ohno, N. Usami, *J. Appl. Phys.* **2022**, 132, 025102.
- [65] J. Canny, *IEEE Trans. Pattern Anal. Mach. Intell.* **1986**, PAMI-8, 679.
- [66] I. Arganda-Carreras, V. Kaynig, C. Rueden, K. W. Eliceiri, J. Schindelin, A. Cardona, H. Sebastian Seung, *Bioinformatics* **2017**, 33, 2424.
- [67] D. Comaniciu, P. Meer, *IEEE Trans. Pattern Anal. Mach. Intell.* **2002**, 24, 603.
- [68] M. A. Groeber, M. A. Jackson, *Integr. Mater. Manuf. Innov.* **2014**, 3, 56.
- [69] J. B. Wachtman, W. E. Tefft, D. G. Lam, C. S. Apstein, *Phys. Rev.* **1961**, 122, 1754.
- [70] J. Vanhellemont, A. K. Swarnakar, O. Van der Biest, *ECS Meet. Abstr.* **2014**, MA2014-02, 1664.
- [71] P. B. Hirsch, *Electron Microscopy of Thin Crystals*, Butterworth, Washington **1965**, ch. 11.
- [72] P. E. Blöchl, *Phys. Rev. B* **1994**, 50, 17953.
- [73] G. Kresse, D. Joubert, *Phys. Rev. B* **1999**, 59, 1758.
- [74] G. Kresse, J. Furthmüller, *Comput. Mater. Sci.* **1996**, 6, 15.
- [75] G. Kresse, J. Furthmüller, *Phys. Rev. B* **1996**, 54, 11169.
- [76] J. P. Perdew, A. Ruzsinszky, G. I. Csonka, O. A. Vydrov, G. E. Scuseria, L. A. Constantin, X. Zhou, K. Burke, *Phys. Rev. Lett.* **2008**, 100, 136406.
- [77] R. Dronskowski, P. E. Bloechl, *J. Phys. Chem.* **1993**, 97, 8617.
- [78] M. Küpers, P. M. Konze, S. Maintz, S. Steinberg, A. M. Mio, O. Cojocaru-Mirédin, M. Zhu, M. Müller, M. Luysberg, J. Mayer, M. Wuttig, R. Dronskowski, *Angew. Chem., Int. Ed.* **2017**, 56, 10204.
- [79] S. Maintz, V. L. Deringer, A. L. Tchougréeff, R. Dronskowski, *J. Comput. Chem.* **2016**, 37, 1030.